Title	MXene nanosheet/organics superlattice for flexible thermoelectrics
Authors	Wang, Zhiwen;Chen, Mengran;Cao, Zhining;Liang, Jia;Liu, Zhenguo;Xuan, Yuxue;Pan, Lin;Razeeb, Kafil M.;Wang, Yifeng;Wan, Chunlei;Zong, Peng-an
Publication date	2022-11-01
Original Citation	Wang, Z., Chen, M., Cao, Z., Liang, J., Liu, Z., Xuan, Y., Pan, L., Razeeb, K. M., Wang, Y., Wan, C. and Zong, P. (2022) 'MXene nanosheet/organics superlattice for flexible thermoelectrics', ACS Applied Nano Materials. doi: 10.1021/acsanm.2c03813
Type of publication	Article (peer-reviewed)
Link to publisher's version	10.1021/acsanm.2c03813
Rights	© 2022, American Chemical Society. This document is the Accepted Manuscript version of a Published Work that appeared in final form in ACS Applied Nano Materials, after technical editing by the publisher. To access the final edited and published work see: https://doi.org/10.1021/acsanm.2c03813
Download date	2025-01-28 12:51:27
Item downloaded from	https://hdl.handle.net/10468/13883

MXene Nanosheet/Organic Superlattice for Flexible Thermoelectrics

Journal:	*ACS Applied Nano Materials*
Manuscript ID	an-2022-03813g.R2
Manuscript Type:	Article
Date Submitted by the Author:	19-Oct-2022
Complete List of Authors:	Wang, Zhiwen; Nanjing Tech University, School of Materials Science and Engineer Chen, Mengran; Nanjing Tech University, School of Materials Science and Engineer Cao, Zhining; Nanjing Tech University, School of Materials Science and Engineer Liang, Jia; Tsinghua University, School of Materials Science and Engineer Liu, Zhenguo; Shenzhen Research Institute of Northwestern Polytechnical University; Northwestern Polytechnical University, Institute of Flexible Electronics; Ningbo Institute of Northwestern Polytechnical University Xuan, Yuxue; Ningbo Institute of Northwestern Polytechnical University Pan, Lin; Nanjing Tech University, School of Materials Science and Engineer Razeeb, Kafil; Tyndall National Institute, Micro-Nano Systems Centre Wang, Yifeng; Nanjing Tech University, School of Materials Science and Engineer Wan, Chunlei; Tsinghua University, School of Materials Science and Engineer Zong, Peng-an; Nanjing Tech University, School of Materials Science and Engineer

SCHOLARONE™
Manuscripts

MXene Nanosheet/Organic Superlattice for Flexible Thermoelectrics

Zhiwen Wang[a], Mengran Chen[a], Zhining Cao[a], Jia Liang[b], Zhenguo Liu[c], Yuxue Xuan[c], Lin Pan[a],

Kafil M. Razeeb[d], Yifeng Wang[a], Chunlei Wan[b], Peng-an Zong[a,c,*]

[a] College of Materials Science and Engineering, Nanjing Tech University, Nanjing 210009, China

[b] State Key Laboratory of New Ceramics and Fine Processing, School of Materials Science and Engineering, Tsinghua University, Beijing 100084, China

[c] Key Laboratory of Flexible Electronics of Zhejiang Province, Ningbo Institute of Northwestern Polytechnical University, Ningbo 315103, China

[d] Micro-Nano Systems Centre, Tyndall National Institute, University College Cork, Dyke Parade, Lee Maltings, Cork T12 R5CP, Ireland

* Corresponding Author:

Dr. Peng-an Zong (georgepazong@gmail.com)

Abstract: 2-dimensional (2D) materials with outstanding electronic transport properties, are rigid against bending due to strong in-plane covalent bonding, and intrinsically flexible due to lack of out-of-plane constrain, thus have been considered promising for flexible thermoelectrics. As a typical 2D material, MXene, however exhibited restricted thermoelectric performance, because the termination groups and guest molecules in MXene nanosheets introduced by acid etching and reassembly deteriorate intra/inter-flake conduction. This work realized increase in both carrier concentration as well as intra/inter-flake mobility by construction of the MXene nanosheet/organic superlattice and composition engineering, attributing to the electron injection, intercoupling strengthening, as well as defect reduction at nanosheet-edges. An electrical conductivity increased by 5 times, to 2.7×10^5 S m^{-1}, led the power factor up to ~33 μW m^{-1} K^{-2}, which is above the state of the art for similar materials, almost by a factor of ten. A thermoelectric module comprising four superlattice film legs could yield 58.6 nW power at a temperature gradient of 50 K. Additionally, both the annealed film and the corresponding module exhibited excellent reproducibility and stability. Our results provide a strategy to tailor the thermoelectric performance of 2D-material films through superlattice construction and composition engineering.

Keywords: MXene, nano sheet, intercalation, superlattice, thermoelectric, flexibility

1. Introduction

By converting skin heat into electricity based on the Seebeck effect, flexible thermoelectrics (TEs) have the potential to provide long-lasting and reliable power for wearable electronics, such as smart watches, fitness trackers, and medical sensors, etc. Compared with traditional lithium-based batteries, flexible TEs are free of safety concerns, because they are maintenance free and need no on-grid recharging. Therefore, they have been attracting intensive research interests.[1-3] The conversion efficiency of TE devices is determined by the TE figure of merit,[4] $zT = S^2\sigma T/\kappa$, where, S is Seebeck coefficient, σ is electrical conductivity, T is the absolute temperature and κ is the thermal conductivity; the comprehensive electronic transport indicator is termed as power factor, $PF = S^2\sigma$. Besides owning good TE performance, TE materials are required to be lightweight, non-toxic as well as flexible for wearable applications.

Although the ductile inorganic materials, typically, Ag(Cu)-S(Se/Te) system, revealed excellent flexibility and TE performance,[5-7] most conventional bulk or 3-dimensional (3D) inorganic materials, such as Bi_2Te_3, $CoSb_3$, PbTe, SiGe, etc. are usually rigid and brittle due to covalent/ionic bonding. However, they can become flexible, when made thin enough. Typically, crystalline silicon based microelectronics can become flexible at a thickness of ~0.1 mm.[8] Therefore, depositing a thin layer of inorganic materials onto flexible substrates or into porous structures can achieve a certain degree of flexibility as well as good TE performance. Recently, Shi et al.[9] synthesized Bi_2Te_3/nickel foam composite film by depositing nano-sized Bi_2Te_3 into the nickel foam by hydrothermal method, which revealed good flexibility and an increased PF. Loureiro et al.[10] deposited the low-cost, earth-abundant and environmentally-friendly material — Aluminum Zinc Oxide (AZO) by radio frequency and pulsed direct current magnetron sputtering. An improved PF of ~400 μW m^{-1} K^{-2} was

achieved, which may be applied in low power consumption electronic devices. Organic materials, typically conductive polymers, though being flexible due to their chain-structures, are strongly restricted in electronic transport properties, ascribing to the hopping conducting nature. Developing composite materials, specifically nanocomposites based on organic/inorganic compositing has been proven to be an effective strategy to achieve the best of both worlds, namely good electrical transport properties of inorganics and excellent flexibility/low thermal conductivities of organics. For example, Figueira et al.[11] fabricated a flexible, scalable, and efficient TE touch detector based on PDMS/graphite flakes composite.

Compared with 3D materials, 2-dimensional (2D) materials, such as atomically thin graphene, black phosphorus, transition metal dichalcogenide (TMDC), are rigid against the bending due to strong in-plane covalent bonding, but intrinsically flexible due to lack of out-of-plane constrain[12,13] and exhibit excellent electronic transport properties.[14] Therefore, they are promising for practical flexible TE devices. Among them, transition metal carbides or nitrides (MXenes) have been widely investigated in areas such as energy storage,[15-18] catalysts,[19-21] electromagnetic shielding,[22-24] sensor,[25] and among others, since its discovery in 2011,[26] due to excellent electrochemical activity, hydrophilicity, electrical conductivity, etc.[27,28] MXenes are conventionally prepared by selective removing the A atoms from the layered parent ternary carbide compounds (MAX), e.g., Ti_3AlC_2 (MAX) $\rightarrow Ti_3C_2T_x$ (MXene), where T is the surface termination groups, such as -O, -OH, -F and -Cl.[29,30] The general formula of MAX is $M_{n+1}AX_n$, where M is the transition metal atoms (e.g. Ti, Nb, Mo, Cr or Ta), A is the atoms belonging to groups 13 and 14 element in periodic table (e.g. Al, Si, S, P, Sn or Ge), X is C and/or N, and n =1, 2, or 3.[31,32] In MAX, each X atomic layer is sandwiched by two M atomic layers, while the A atomic layer is sandwiched by two $M_{n+1}X_n$ layers. Wherein, the

M-A metal bonding is weaker than the M-X covalent bonding.[33-35] To date, more than 30 species of

MXenes,[36] such as Nb_2CT_x, Ti_3NCT_x, etc., have been developed. Among them, $Ti_3C_2T_x$ is

lightweight, non-toxic, flexible, and thus is the most widely investigated.

One of the important factors that restricting the TE performance of $Ti_3C_2T_x$ is that the surface

termination groups, interlayer guests in MXene introduced by acid etching and assembly would

increase both intra-flake and inter-flake resistance. Because $Ti_3C_2T_x$ was synthesized in a strong acid

solution, typically, in HCl/LiF aqueous solution,[37] the emergent surface functional groups -T with a

strong electron affinity,[38,39] would trap electrons. The $Ti_3C_2T_x$ film was usually obtained by

subsequent vacuum filtration method, which would form structural defects (vacancies and holes),[40,41]

physically/chemically bound H_2O[42] in the interspace and TiO_2 at the nanosheet edges.[43] The

physically-bound water can get removed by low-temperature heating, whereas the complete

elimination of chemically-bound water demands higher temperatures ($\geq$300 °C).[44] The interlayer

H_2O was considered to oxidize Ti into TiO_2 at the nanosheet edges, where the atomic activity is

higher.[45] As the 2D nanosheet edges are important conduction channels for intra-flake electron

transmission, the presence of H_2O and generated TiO_2 would scatter electrons, and seriously

deteriorate the carrier mobility.[46]

Organic intercalation into some layered inorganic TE materials has been proven effective in

co-optimization of TE performance and flexibility. One of the vital mechanisms for TE-performance

optimization is the electron injection effect.[6,47,48] For example, after intercalation of hexylamine (HA)

molecules into the interspace, the lone pair electrons of N atoms in the $-NH_2$ group of HA would

inject electrons into the inorganic layers,[49] thus increasing the carrier concentration. Therefore,

intercalation of ionic organics is expected to enhance the carrier concentration of MXene films by

similar mechanism. However, organic intercalation would expand the interlayer distance, weakening the coupling between adjacent layers, thus increasing the inter-flake resistance. It is thus important to realize co-optimization of carrier concentration as well as mobility.

Herein, we have constructed the $Ti_3C_2T_x$ nanosheet/organic superlattice (SL) by a facile exfoliation-self-assembly method, in the hope of increasing carrier concentration by electron injection effect. After that, we have carried out post-annealing at different temperatures for tuning of intercalating composition as well as interlayer distance, with the expectation of strengthening interlayer-coupling, edge-oxide elimination for increasing inter-flake and intra-flake mobility, and structural stabilization. The synthesis, microstructures, TE properties as well as the underlying mechanisms have been discussed.

2. Experimental

2.1 Synthesis

Synthesis of $Ti_3C_2T_x$/organics SL film and fabrication of TE module: firstly, as shown in **Figure 1**, the etching solution was prepared by adding 1.6 g lithium fluoride (LiF, 99%, Macklin) into 20 mL 9 M hydrochloric acid (HCl, Yonghua Fine Chemical) under stirring at room temperature. Then, 1 g Ti_3AlC_2 powder (200 mesh, 98%, Macklin) was slowly added into the LiF/HCl solution under stirring. The mixture was kept at 50 °C for 24 h. The resulting suspension was washed with deionized (DI) water by repeated centrifugation at 5000 rpm for 5 min per cycle (TG16-WS Centrifuge, Cence) until its pH reached 6-7. Then, the precipitate was vacuum dried at 60 °C for 12 h to obtain $Ti_3C_2T_x$ powder. After that, 1 g $Ti_3C_2T_x$ powder was dispersed into 10 mL DI water under ultrasonication in the ice-water bath for 10 min. The mixture was centrifuged at 3500 rpm for 5 min to obtain the supernant, which was transferred into a Petri dish and vacuum-dried at 120 °C to obtain

the $Ti_3C_2T_x$ film (referred to as MX). Additionally, 0.2 g $Ti_3C_2T_x$ powder was manually ground with

slowly added 1 mL HA (99%, Energy Chemical) for 30 min in an agate mortar. The mixture was

transferred into 20 mL N-methylformamide (NMF, 99%, Macklin) and ultrasonicated in ice-water

bath for 10 min, followed by centrifugation at 3500 rpm for 5 min. The supernant was then

transferred into a Petri dish and vacuum-dried at 140 °C for 3 h to obtain the flexible

$Ti_3C_2T_x$/organics hybrid SL films (referred to as MX SL film). The MX SL films were then annealed

at 300, 400 and 500 °C for 1 h, to obtain MX SL-300, MX SL-400 and MX SL-500 films,

respectively. In this work, 3 batches of MX, MX SL, SL-300, SL-400 and SL-500 films were

prepared. For each composition in each batch, 3 samples were cut out from different regions. As

shown in **Figure S1**, for a specific composition, the fluctuation of σ and S was within 5% and 10%,

respectively, in the same batch; while they increased to be within 10% and 15% from batch to batch,

implying good reproducibility and reliability of the process. Four legs with a dimension of 2 cm

(length) × 0.5 cm (width) × ~8 μm (thickness) were cut out from the MX SL-400 SL film, and placed

thermally in parallel on a piece of tape. They were connected electrically in series with silver paint to

form a simple TE module.

2.2 Characterization

Phases, compositions and microstructures: Phase structures were characterized by X-ray

diffraction (XRD, SmartLab, Rigaku) equipped with CuK_α radiation (λ = 0.154 nm) at room

temperature in air. The cross-sectional microstructures of the SL films were investigated by a

scanning electron microscopy (SEM, HITACHI Regulus 8220) equipped with energy dispersive

X-ray spectroscopy (EDS, Oxford), and a transmission electron microscopy (TEM, JEM-2010) at

room temperature in vacuum. Chemical composition and bonding were further analyzed using X-ray

photoelectron spectroscopy (XPS, Thermo Scientific K-Alpha) setup with a monochromated AlK$_\alpha$ X-ray source (hv = 1486.6 eV) at room temperature in vacuum. Binding energies were referenced to the C 1s peak, which located at 284.6 eV. The XPS data were analyzed using a professional software (AVANTAGE). Thermal gravity analysis (TG) was carried out on a thermogravimetric analyzer (NETZSCH STA 449F3) from room temperature to 600 °C at a heating rate of 10 °C /min in N$_2$ with flow rate of 50 mL/min.

Physical properties: A commercial Hall Effect Measurement System (CH-Magnetoelectricity Technology, CH-100) with a magnetic field of 500 mT was used to characterize the in-plane carrier concentration/mobility, and electrical conductivity of the hybrid SL films at room temperature (**Figure S2a**). A home-made thin-film Seebeck coefficient test device was utilized to measure the Seebeck coefficient. As shown in **Figure S3**, the voltage gradient (ΔV) and temperature gradient (ΔT) were measured simultaneously after establishing a temperature gap with two inversely placed Peltier chips. The Seebeck coefficient was then computed by linear regression of ΔV *vs.* ΔT with a high linear correlation coefficient ($R^2 > 99\%$). The flexibility of the SL films was measured by fitting the samples closely onto the outside surfaces of different glass tubes with decreasing radius and assessing the change rate of resistivity by a Four-Point Probe System (Lriper, LPPS100A). The in-plane thermal conductivity (κ) was computed by $\kappa=\rho C_p\lambda$, where C_p is the specific capacity, ρ is the density, λ is the thermal diffusivity measured on a thermal diffusivity analyzer (ai-phase Mobile M3) at room temperature. The mean measurement errors of electrical conductivity, Seebeck coefficient and thermal conductivity were within 3%, 5% and 5%, respectively.
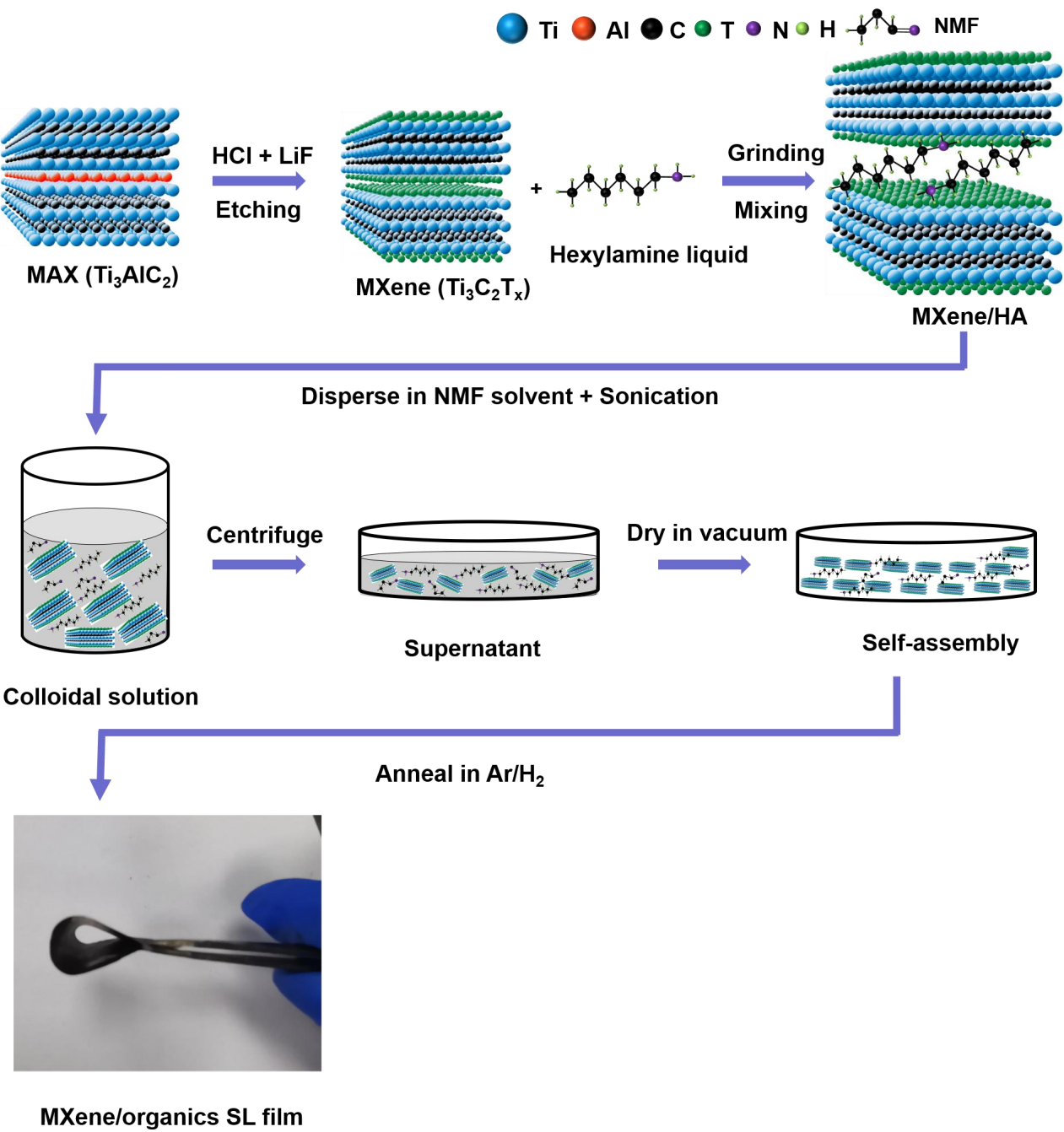
Figure 1. Schematic diagram of the synthesis of the MXene/organics hybrid SL film by an intercalation-exfoliation-reassembly method.

3. Results and discussions

3.1 Phase and microstructure

The synthesis route of the MXene/organics hybrid SL film was schematically shown in **Figure**

1. Firstly, the Al atomic layers in parent Ti_3AlC_2 powder were selectively etched by LiF/HCl aqueous solution according to Equation (1):[50]
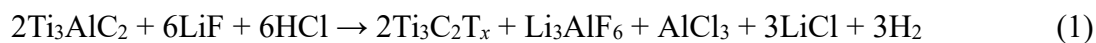
$$2Ti_3AlC_2 + 6LiF + 6HCl \rightarrow 2Ti_3C_2T_x + Li_3AlF_6 + AlCl_3 + 3LiCl + 3H_2 \qquad (1)$$

As shown in **Figure 2a**, the disappearance of (104) peak ($2\theta = 39°$) in Ti_3AlC_2 confirmed the removal of Al atoms. After etching, the MXene layers would be decorated with surface termination groups, including -OH, -O, -F and -Cl, as well as chemically/physically bound H_2O. The interlayer distance was thereby increased from 9.05 Å to 9.76 Å according to Bragg's equation (*2dsinθ = nλ*), corresponding to the left-shifting (9.76° to 9.04°) of the (002) peak (**Figure 2c-d**). By grounding MXene powder in sufficient amount of HA, the HA molecules were intercalated into the interlayer gaps, generating swelled MXene/HA powder (MX/HA). The interlayer distance was sharply increased to 24.1 Å, corresponding to much-decreased *2θ* (9.04° to 3.66°). Because HA molecule is of a length of 10.44 Å and a width of 1.78 Å,[51] while the expanded distance (14.3 Å) was smaller than twice of its length, it can be inferred that HA molecules form a paraffin-like bilayer structure with a 43° inclination (**Figure S4a**). However, the MXene/HA/NMF film (MX SL film) synthesized by exfoliating MXene/HA in NMF and subsequent reassembly, exhibited a slightly right-shifting of (002) peak (3.66° to 6.28°), indicating a narrowed interlayer distance to 14.06 Å, due to substitution NMF for partial HA. That is, during the exfoliation-reassembly process, some HA molecules were de-intercalated, whereas some NMF molecules was inserted due to the solvent effect. As the NMF molecule is of 4.13 Å long and 2.31 Å wide, which is smaller than HA, it can thus be inferred that HA molecules aligned with a 24° inclination in the gap (**Figure S4b**).
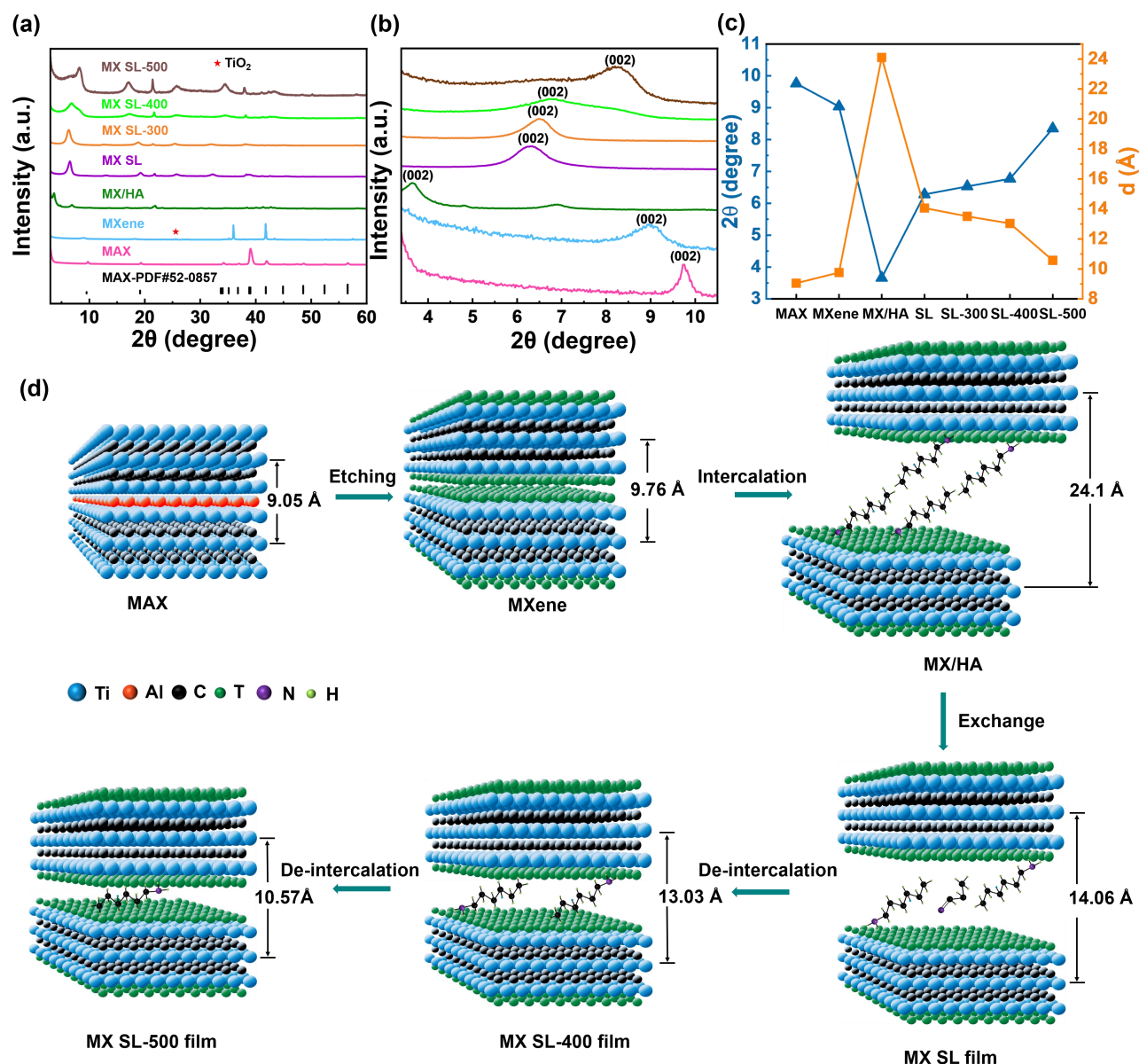
Figure 2. The XRD patterns (a), the (002) peak region (b), the interlayer distance, d *vs*. 2θ (c) of Ti$_3$AlC$_2$, MXene, MX/HA, unannealed MX/HA/NMF (MX SL) and MX SL annealed at 300 °C, 400 °C and 500 °C, which were referred to as MX SL-300, MX SL-400 and MX SL-500, respectively; (d) schematic diagram of the structural changes from MAX to MXene, MX/HA, MX SL, MX SL-400 and MX SL-500 films.

After annealing MX SL film at 300, 400 and 500 °C, the (002) peaks of the corresponding films, MX SL-300, MX SL-400 and MX SL-500, right-shifted to 6.53°, 6.77° and 8.35°, implying a gradually narrowed interlayer distances to 13.51 Å, 13.03 Å and 10.57 Å, respectively, which was attributed to the gradual elimination of intercalated guests. However, the SL films have similar XRD spectra before and after annealing, manifesting that the post-annealing process did not damage the SL structure. The vacuum-dried MX SL film peeled off from the bottom of petri dish, exhibited a smooth surface (**Figure S5a**), signifying the formation of a dense structured film. The self-supporting film was intrinsically flexible, as it could be easily bent without binder-additives as shown in **Figure S5b**. **Figure 3a** showed the cross-sectional microstructure of the MX SL film, the wavily aligned morphology was observed, demonstrating appropriate exfoliation and piling of $Ti_3C_2T_x$ nanosheets. The interlayer distance of the MX SL-film was ~1.4 nm according to the cross-sectional TEM observation (**Figure 3b**), agreeing well with the theoretical d-spacing based on Barrage equation. **Figure 3c** showed the full XPS spectra of MXene powder and MX SL film. Compared with MXene powder, the N peak emerged at ~400 eV in the MX SL film, which was due to the intercalation of HA between adjacent MXene nanosheets. In the Ti 2p curves (**Figure 3d and 3e**), the peak locating at ~454.8 eV (~456.0 eV) was ascribed to Ti-N bond,[52,53] corresponding to the N-Ti peak (~397.2 eV) in the N 1s region (**Figure 3f**), implying that an ionic bonding was formed between HA and the MXene nanosheets. Since MXene has empty Ti 3d orbitals, it can receive electrons from the nitrogen atoms in the grinding process, thus could get negatively charged. Meanwhile, the organic cations (HA$^+$) were intercalated into the van der Waals gap of MXene by the electrostatic force.
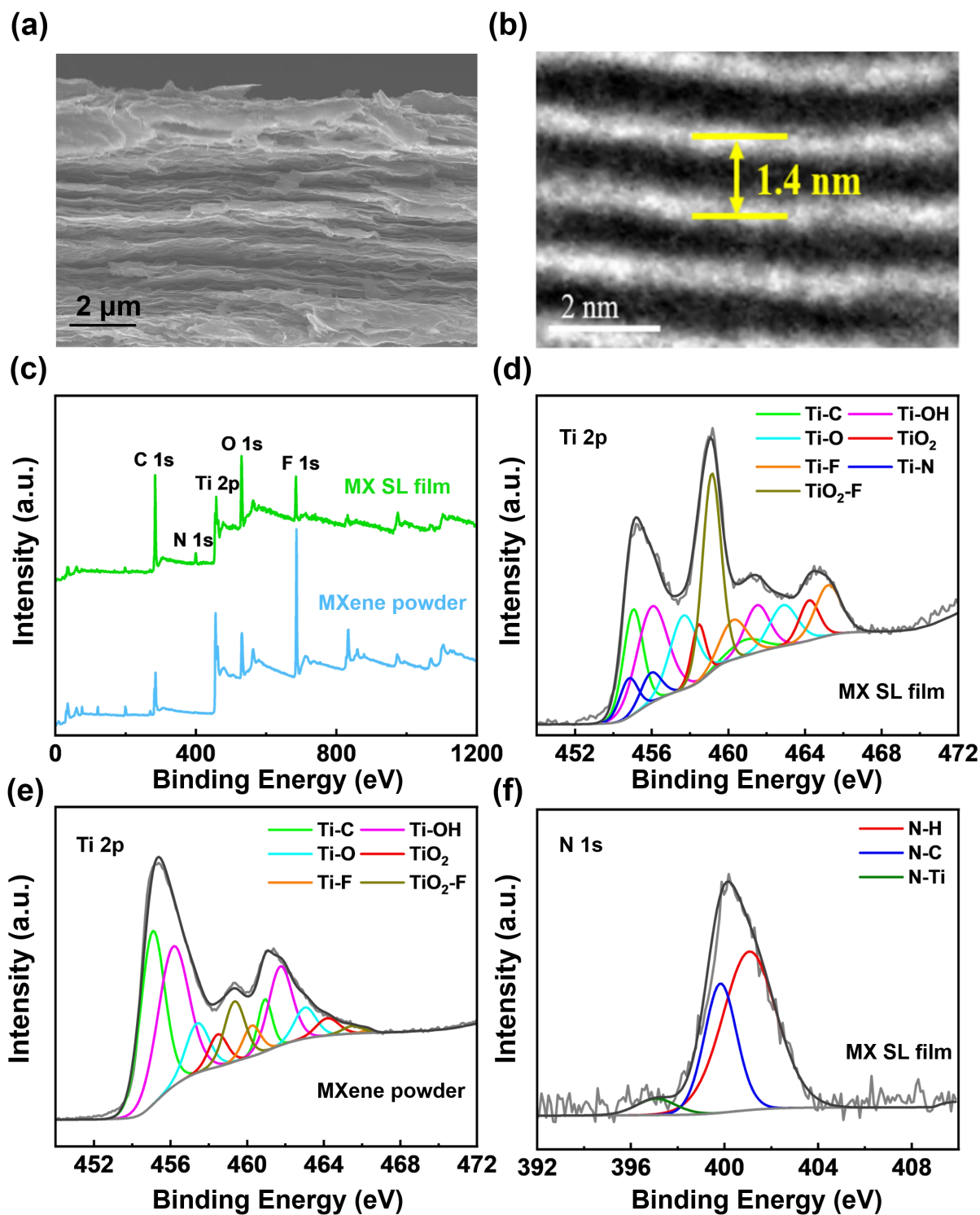
Figure 3. (a) Cross-sectional SEM and (b) high-resolution TEM images of the MX SL film; (c) XPS survey of the MX SL film and MXene powder; XPS spectrum of Ti 2p region for the (d) MX SL film, (e) MXene powder, and (f) N 1s region of MX SL film.

To investigate the influence of post-annealing on the composition of interlayer guests, the surface detection technology — XPS was performed on the MX SL films before and after post-annealing at different temperatures. The main elements of Ti, C, F, O and N were observed in the survey scan (**Figure 4a**). The relative peak intensity of the F, O and N elements were decreased after annealing, agreeing well with the decreased corresponding atomic ratios (**Figure 4b**), which was suggested to be due to the breakage of some Ti-F bonds, removal of H_2O and intercalated organics (HA, NMF). As shown in **Figure 4c**, the spectra of N 1s region was splitted into peaks assigned to N-H (~401.1eV), N-C (~399.8eV) and N-Ti (~397.2eV), respectively.[54] **Figure 4d** showed the deconvolution results of the O 1s region, where the O 1s spectra was splitted into peaks assigned to Ti-O (~530 eV), C-Ti-O (~531 eV), C-Ti-OH (~532 eV), C-O (~532.8 eV), H_2O (~533.8 eV) and TiO_2 (~530.5 eV),[52] respectively. It was also observed that the fraction of N-Ti was reduced from 13.8% to 2.7% after annealing at 500 °C (**Figure 4e**), which was consistent with the decrease in the N atomic percentage in Figure 4b. The fraction of H_2O and TiO_2 was reduced after annealing and the H_2O disappeared after annealing at 400 °C (**Figure 4f**), which was also in line with the decrease in the O atomic percentage in **Figure 4b**. And the integral peak ratio of C-Ti-O was increased from 34.2% to 65% after annealing at 400 °C. On the contrary, the integral peak ratio of C-Ti-OH was decreased from 39.2% to 29.2%.
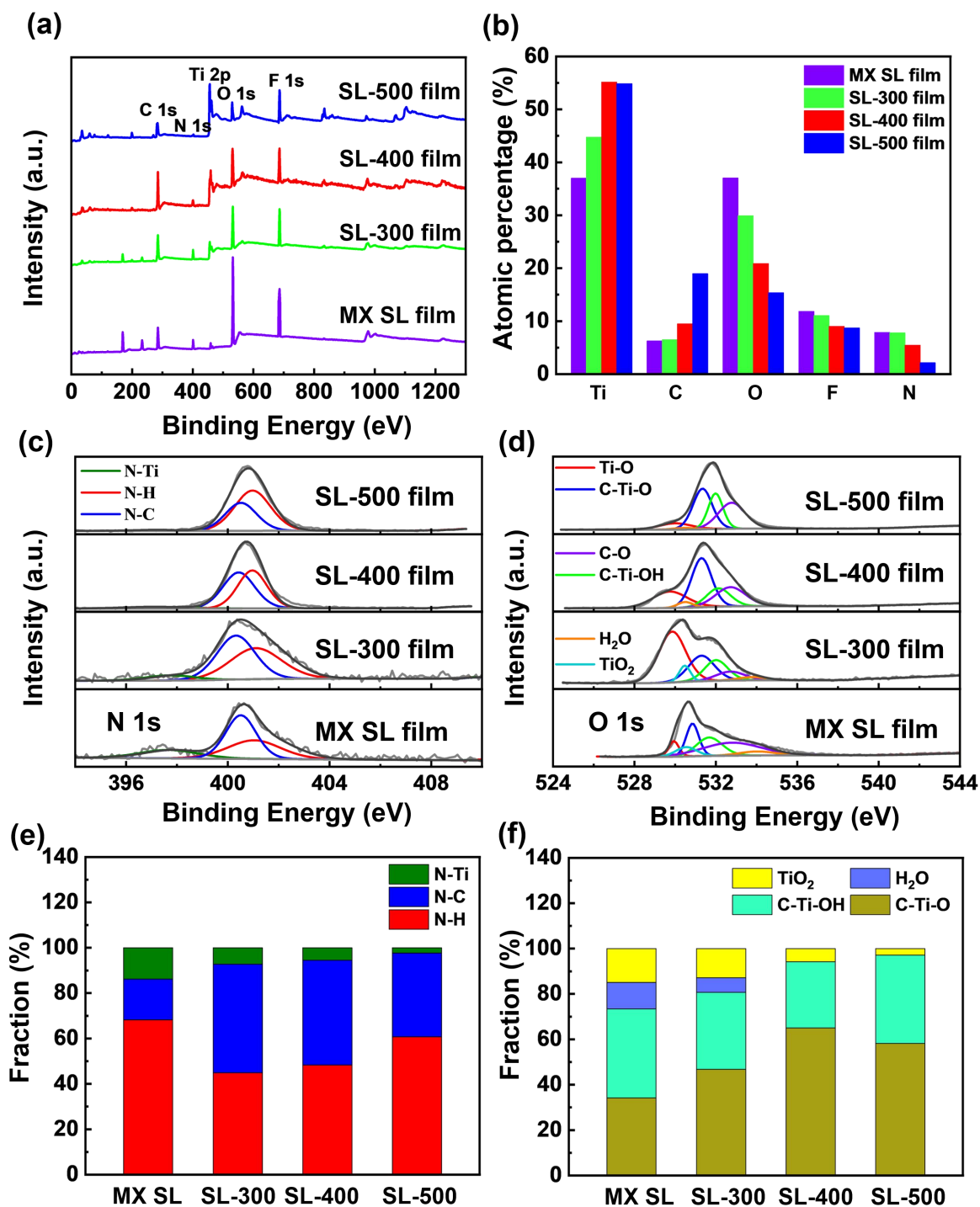
Figure 4. XPS survey scan (a); the atomic percentage (b); peak deconvolution of the N 1s (c) and O

1s region (d), fractions of the fitted moieties in N 1s (e) and O 1s region (f) for MX SL, MX SL-300,

MX SL-400 and MX SL-500 films.

3.2 Thermoelectric properties

The electrical conductivity, σ, Seebeck coefficient, S, carrier concentration, n and mobility, μ of the films are shown in **Figure 5a-c**, respectively. The σ of the vacuum-dried MX film was 0.5×10^5 S m^{-1}, much lower than the defect-free of MXene single-layer (6.5×10^5 S m^{-1}),[55] because etching was considered to produce structural defects, such as vacancies/holes inside the MXene nanosheets,[56,57] due to the strong acidity of solution medium. Moreover, as the nanosheet edges are more active than inner regions, Ti atoms nearby the edges were readily oxidized by O from H_2O to be TiO_2, according to Equation (2):[44]

$$Ti_3C_2O_2 + 4H_2O \;\rightarrow\; 3TiO_2 + 2C + 4H_2 \tag{2}$$
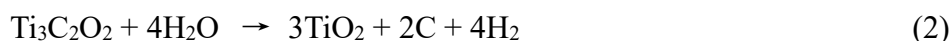
The formed TiO_2 at the nanosheet edge was considered to hinder the carrier transport, as the nanosheet edges are significant conduction channels. The intra-flake resistance would thereby increase. After organic intercalation, the σ of the MX SL film was increased to 0.8×10^5 S m^{-1}, due to elevated n, because Ti in MXene has empty 3d orbitals, which can accept electrons from guests; and HA molecules could act as electron donors due to the existence of lone pairs of electrons in nitrogen atoms (**Figure 5d**). Electrons could thus transfer from the HA molecules to MXene. However, the μ was reduced slightly, because the entry of organics expanded the interlayer distance, weakened the inter-flake coupling, thus hindering the inter-flake carrier transport. After organic intercalation, the S did not change remarkably, while the PF increased from 4.2 μW m^{-1} K^{-2} of MX film to 7.5 μW m^{-1} K^{-2} of MX SL film, corresponding well to the trend of σ.

The etching as well as subsequent organic intercalation could introduce surface termination groups and organics, and increase the interlayer distance, thus weakening the inter-layer coupling and hindering the inter-flake carrier transmission. In addition, the presence of TiO_2 at the nanosheet

edges could also add to the hindrance of intra-flake carrier transport (**Figure 5e**). All the above

factors would reduce μ of the MX SL film. Post-annealing can be used to weaken the above negative

factors. The MX SL films were annealed at 300 °C, 400 °C, and 500 °C in H_2 atmospheres, the

obtained films were referred to as MX SL-300, MX SL-400 and MX SL-500, which showed

increased σ to 1.7 , 2.7 and 2.4×10^5 S m^{-1}, respectively.
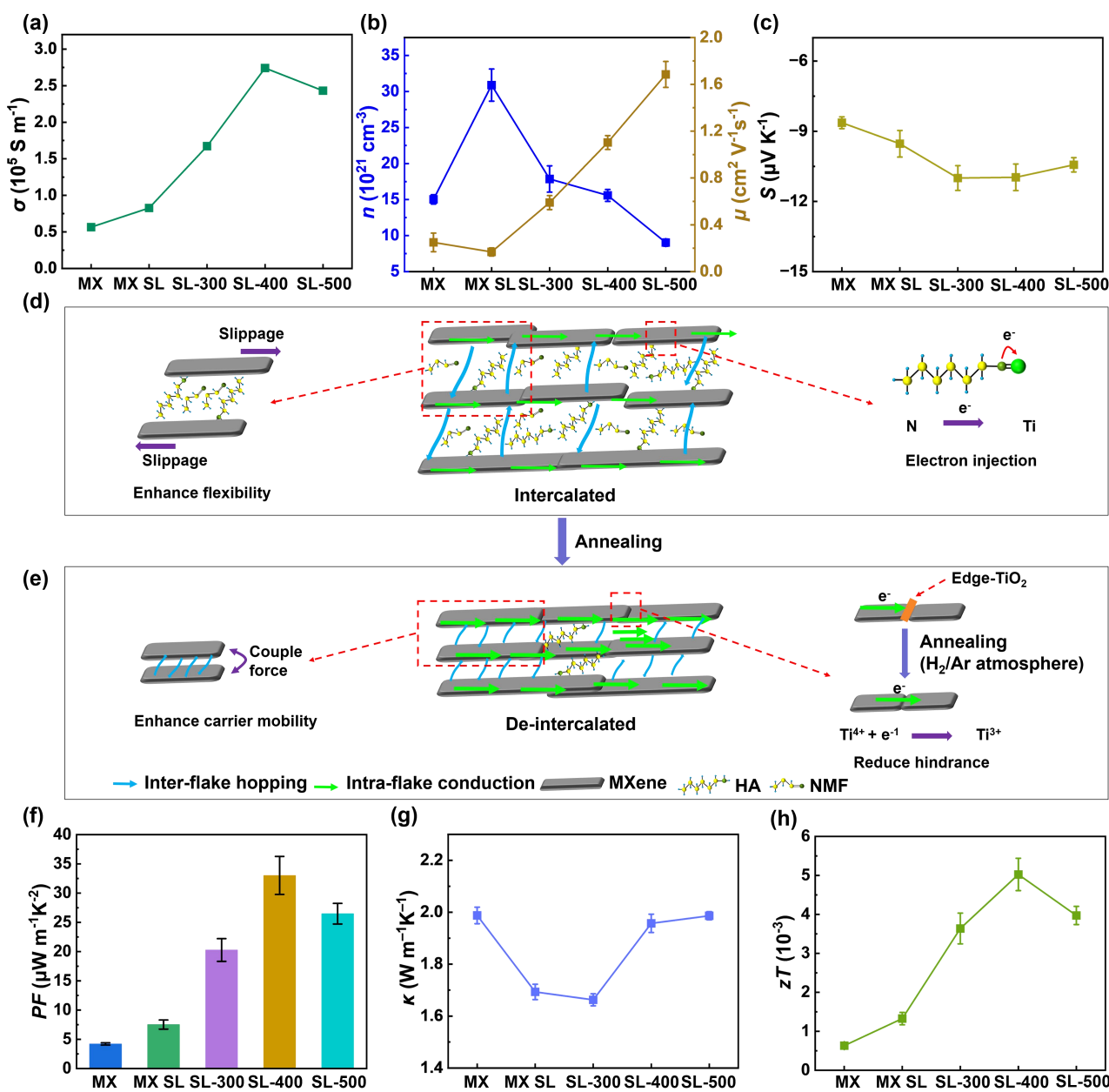
Figure 5. (a) Electrical conductivity, σ; (b) Carrier concentration, n and mobility, μ; (c) Seebeck

coefficient, *S*; (d) and (e) Schematic diagrams of the mechanisms that how SL construction and composition engineering affect the flexibility, carrier concentration as well as mobility; (f) Power factor, *PF*; (g) Thermal conductivity, *κ*; (h) *zT* value of MX, MX SL, SL-300, SL-400 and SL-500 films.

As shown in **Figure 5c**, the *n* of the MX SL film decreased while the *μ* increased with increasing annealing temperature. The decrease in *n* was due to weakening of the electron injection effect, as result of the gradual de-intercalation of HA at high temperatures. The increase in *μ* was due to the concurrent reduction of inter-flake and intra-flake hindrance. With the increase of annealing temperature, the H_2O, termination groups and organics in MXene interlayer would be gradually removed from the MXene interlayer, thus decreasing the interlayer distance, strengthening layer-to-layer coupling, leading to reduction of the carrier transmission barriers. The intra-flake hindrance was also reduced due to restoration from Ti^{4+} to Ti^{3+}. As revealed by XPS, TiO_2 at the nanosheet edges was considered to get electrons from H_2 and get reduced ($Ti^{4+} \rightarrow Ti^{3+}$), according to Equation (3):[58]

$$2Ti^{4+} + O^{2-} + H_2 \rightarrow 2Ti^{3+} + V_o + H_2O \tag{3}$$

where, V_o means O vacancy. As the transport channels were restored, the inter-flake *μ* was thus increased.

For metals or heavily doped semiconductors, the *S* would decrease with increase in *n*, according to the Mott equation,[59] $S = \frac{8\pi^2\kappa_B^2 T}{3eh^2} m^* \left(\frac{\pi}{3n}\right)^{2/3}$, where κ_B is Boltzmann constant, *h* is Planck constant, and m^* is the effective mass, *e* is elementary charge. According to **Figure 5b** and **5c**, the *S* of the MX SL films did not change significantly with increased *n*, because Mott equation was considered not inapplicable here due to the composite nature of the MX SL films. Hicks and Dresselhaus[14] proposed

that low-dimensionality could lead to enlarged S essentially due to surface state effect. However, in

this work, the SL films were of micro-meters thick, stacked by decorated 2D MXene. Therefore, the

impact of surface state on its TE performance was considered not remarkable. Compared with the

MX film, the PF of the MX SL-400 film was increased by over 8 times and reached the peak value

of ~33 μW m^{-1} K^{-2} (**Figure 5f and Table 1**). The PFs of the MX SL-300 film and MX SL-500 film

were 20.2 and 26.3 μW m^{-1} K^{-2}, which was in line with the trend of σ.

Table 1. Key parameters of the structure and TE properties of MX, MX SL, SL-300, SL-400 and

SL-500 films.

Sample	2θ (°)	d (Å)	σ (10⁵ S m⁻¹)	S (μV K⁻¹)	PF (μW m⁻¹ K⁻²)	κ (W m⁻¹K⁻¹)	zT (10⁻³)
MX SL film	6.28	14.06	0.83	−9.5	7.5	1.69	1.32
SL-300 film	6.53	13.51	1.67	−11	20.3	1.66	3.63
SL-400 film	6.77	13.03	2.74	−10.9	33.0	1.96	5.02
SL-500 film	8.35	10.57	2.43	−10.4	26.8	1.98	3.97

As shown in **Figure 5g**, the in-plane thermal conductivity of the MX SL films (~1.6 W m^{-1}K^{-1})

was reduced compared with that of the MX film (~2.0 W m^{-1}K^{-1}), because the widening of the

acoustic phonon branches after HA intercalation would dampen the acoustic phonon transmission

inside the layers, and organics would severely scatter phonons due to independent vibration.[51] The

removal of HA by annealing was considered to weaken the independent vibration scattering, and the

electronic thermal conductivity was increased due to increased electronic conductivity, thus the

thermal conductivity of SL-400 and SL-500 bounced back. As shown in **Figure 5h**, the maximum

value of zT was thus calculated to be 5×10^{-3} for the SL-400 film. Future work focus on the enhancing its Seebeck coefficient.

3.3 Flexibility and stability

To characterize the flexibility of the films before and after annealing, the MX SL film and MX SL-400 film were bent and kept closed to a series of glass tubes with decreasing radii (**Figure 6a**), and their resistivity at bent state (R_s) was measured and compared with that at flat state (R_0). As shown in **Figure 6b**, the change rate of R_s/R_0 for MX SL and MX SL-400 film was within 10% until a bending radius of 4 mm, indicating excellent flexibility. For MX SL film, after organic intercalation, the increased interspace could provide free space for bending deformation, and the weakened interlayer coupling could make it easier to slide by reducing the slippage barrier between adjacent layers. After post-annealing, the MX SL-400 film still reserved the excellent flexibility, as partial organics still existed in the interspace. Since all inorganic materials can become flexible, when made thin enough, such as ceramics, glasses, etc. It is of essence to consider thickness when quantifying flexibility. Snyder et al.[60] has put forward the concept of figure of merit for flexibility (f_{FOM}) for comparison among thin films with various thickness. The f_{FOM} can be weighed by the yield strain ε, which is the relative elongation on the outer/inner surface determined by geometry: $\varepsilon = h/2r$, where h is the film thickness and r is the critical bending radius upon failure. As shown in **Figure 6c**, the f_{FOM} of the MX SL film was higher than that of a previously reported pure MXene film,[61,62] and comparable to the MXene/organic composites,[63,64] owing to the interspace increment as well as the reduction of slippage barrier.
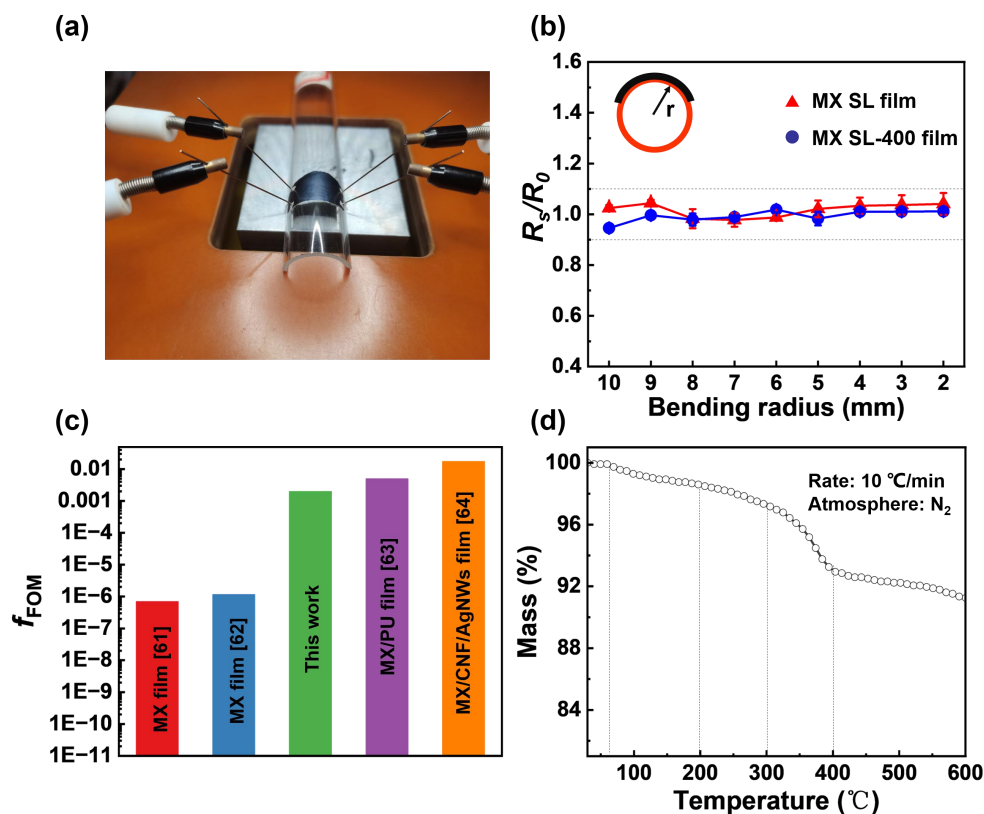
Figure 6. (a) Photograph of flexibility test; (b) the resistivity changes of MX SL film and MX SL-400 film at different bending radius, where R_0, R_s represent the resistivity at flat state and bending state, respectively; (c) the figure of merit for flexibility, f_{FOM} in this work and other reported MX-based film; (d) TG curve of the MX SL film.

The TG curve (**Figure 6d**) exhibited that the MX SL film was considerably stable below 60 ℃, indicating that it would decompose in wearable applications, as the temperature of human skin was ~37 ℃. The weight loss process could be divided into four stages. The first-stage weight loss of 2.5% from 30 to 200 ℃ was considered to be due to the evaporation of the physically-bound water and surface termination -OH.[65] The second-stage weigh loss of 1.3% from 200 to 300 ℃ was attributed to the de-intercalation of NMF and chemically bound H_2O.[66] The third-stage weigh loss of 4.2% from 300 to 400 ℃ was ascribing to the thermal de-intercalation of HA and remaining chemically-bound water.[66] Since the organic cation HA^+ formed ionic bonding with the adjacent

MXene nanosheets, the practical boiling point was improved, compared with that of isolated ones. The fourth stage weigh loss of 1.7% over 400 °C was considered to be attributed to the elemination of the surface termination -F and remaining HA molecules. The air stability of MXene-based films was investigated as shown in **Figure S7**. After being exposed in air (temperature = ~26 °C and relative humidity = ~55%) for 3 months, the decease rates of electrical conductivity for the MX SL-300, MX SL-400 and MX SL-500 films were within 10%, indicating that a good air stability has been achieved by annealing treatment, due to effective removal of moisture and the hydrophilic group -OH.

3.4 Device performance

A simple TE power generation module composed of four single MX SL-400 film legs was fabricated for powering demonstration. The four TE single n-type legs were cleaved onto a flexible tape, and arrayed thermally in parallel and connected electrically in series with silver paste. When one end of the TE module was kept close to the finger skin as the hot side with the other end exposed in the air as the cold side, an output voltage (U) of 0.19 mV could be established (**Figure 7a** and **Figure S6**), implying great potential to power wearable electronics. By attaching the hot end to a heating plate with the cold end sat in the air, and tuning the temperature of the heating plate, different temperature gradients (ΔT) between the two ends could be established. When the ΔT was increased from 10, to 20, 30, 40 and 50 K, the corresponding U was increased from 0.53, to 0.95, 1.33, 1.88 and 2.31 mV, respectively (**Figure 7b and Table 2**). The output power (P) of the TE module could be tested by forming a circuit with auxiliary external resistors. The P was thus calculated based on Equation (2):

$$P = \frac{U^2}{\frac{(R_1-R_2)^2}{R_1}+4R_2} \qquad (2)$$

where R_1 was the external resistance, and R_2 was the internal resistance. Under a fixed ΔT, the P could reach the peak at $R_1 = R_2$. As shown in **Figure 7c**, when ΔT increased from 10 to 20, 30, 40 and 50 K, the corresponding peak P was increased from 2.5 to 10.1, 20.3, 41.0 and 58.6 nW, with corresponding power densities of 0.02, 0.06, 0.13, 0.26 and 0.37 W m^{-2}, respectively (**Figure 7d**). The performance of the TE modules based on SL-400 film legs with the equal dimension from 3 batches was shown in **Table S1**. The mean standard deviation of the P was within 10%, implying good reproducibility. For air stability of the TE module, as shown in **Figure S8**, after being exposed in air (temperature = ~26 °C and relative humidity = ~55%) for 3 months, the P of the module was almost unchanged with less than 5% decrease, revealing excellent stability. This is due to the removal and de-intercalation of most of the organic species, chemically/physically bound water and surface terminated –OH groups during 400 °C annealing, which made the device much more stable. It is expected to drive nano-watt electronic devices, such as sensors, radio communications, signal amplifiers, etc.

Table 2. Room-temperature internal resistance (R_2), maximum output voltage (U), power and power density of the TE module.

ΔT (K)	R_2 (Ω)	U (mV)	Power (nW)	Power density (W m^{-2})
10	27.6	0.53	2.5	0.02
20	25.8	0.95	10.1	0.06
30	22.8	1.33	20.3	0.13
40	21.9	1.88	41.0	0.26
50	20.4	2.31	58.6	0.37
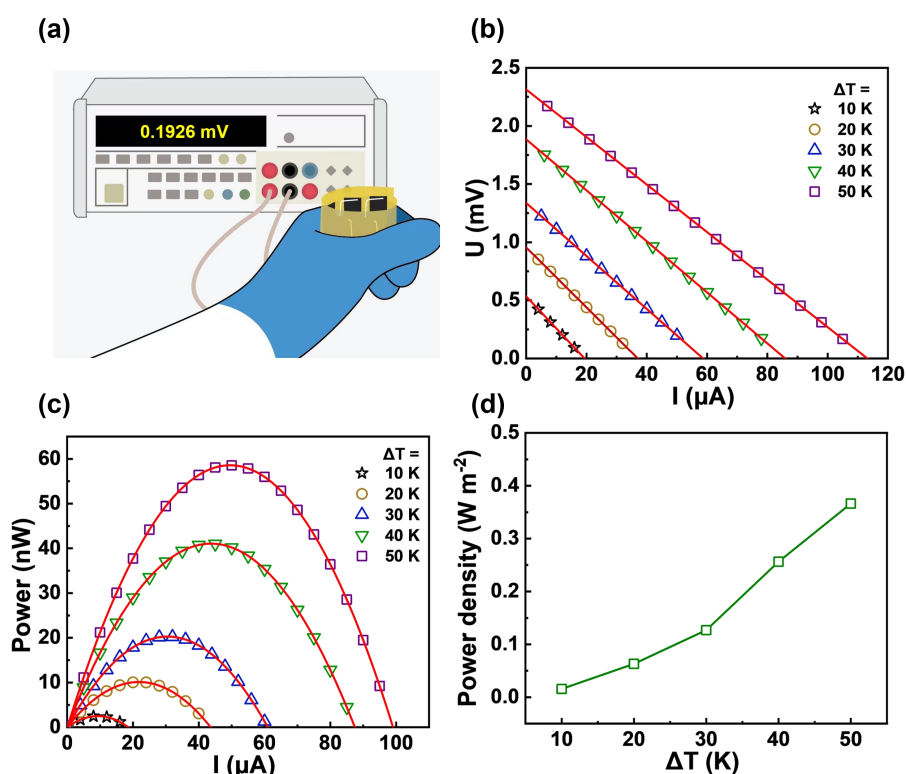
Figure 7. (a) Demonstration of human skin energy harvesting by holding the TE module and measuring the output voltage; (b) output voltage vs. current, (c) output power and (d) power density of the MX SL-400 film based TE module at different temperature differences.

4. Conclusion

In this work, we have constructed the MXene nanosheet/organic superlattice by intercalating HA and NMF, subsequent exfoliation and self-assembly. The formation of superlattice increased the carrier concentration of the MX SL film due to the electron injection effect. The composition engineering by post-annealing increased the carrier mobility by the reduction of both inter-flake and intra-flake hindrance. Thus, the power factor was enhanced over 8 times, to ~33 μW m^{-1} K^{-2}. The 4-legged TE module could generate an output power of 58.6 nW with a power density of 0.37 W m^{-2} at a temperature gradient of 50 K with excellent reproducibility and stability, implying great potential for powering flexible electronics in industry. This work provides a strategy to tailor the TE

performance of MXene based flexible films, which has the potential for large-scale applications.

Conflicts of Interest

The authors declare no conflict of interest.

Supporting Information

Process reproducibility and reliability; setup of Seebeck coefficient and electrical conductivity measurement; molecule alignment after intercalation; molecule alignment after intercalation; film morphology; output voltage of the TE module; air stability of the MXene-based films; reproducibility of the the TE module; and air stability of the TE module.

Acknowledgments

References

(1) Mao, Z. D.; Wang, Z. W.; Shi, T. F.; Zong, P. A.; Liang, J.; Liu, Z. G.; Zhang, P.; Huang, Y. J.; Han, Y.; Ahmad, K.; Almutairi, Z.; Wan, C. L. Sandwiched Graphene/Bi_2Te_3/Graphene Thermoelectric Film with Exceptional Figure of Merit for Flexibility. *Adv. Mater. Interfaces* **2022**, *9*, 2200555. DOI: 10.1002/admi.202200555

(2) Zhu, S. J.; Fan, Z.; Feng, B. Q.; Shi, R. Z.; Jiang, Z. X.; Peng, Y.; Gao, J.; Miao, L.; Koumoto, L. Review on Wearable Thermoelectric Generators: From Devices to Applications. *Energies* **2022**, 15, 3375. DOI: 10.3390/en15093375

(3) Suarez, F.; Nozariasbmarz, A.; Vashaee, D.; Ozturk, M. C. Designing Thermoelectric Generators for Self-Powered Wearable Electronics. *Energy Environ. Sci.* **2016**, *9*, 2099–2113. DOI: 10.1039/c6ee00456c

(4) Bell, L. E. Cooling, Heating, Generating Power, and Recovering Waste Heat with Thermoelectric Systems. *Science* **2008**, *321*, 1457–1461. DOI: 10.1126/science.1158899

(5) Yang, Q. Y.; Yang, S. Q.; Qiu, P. F.; Peng, L. M.; Wei, T. R.; Zhang, Z.; Shi, X.; Chen, L. D. Flexible Thermoelectrics Based on Ductile Semiconductors. Science **2022**, *377*, 854–858. DOI: 10.1126/science.abq0682

(6) Shi, X.; Chen, H. Y.; Hao, F.; Liu, R. H.; Wang, T.; Qiu, P. F.; Burkhardt, U.; Grin, Y.; Chen, L. D. Room-Temperature Ductile Inorganic Semiconductor. *Nat. Mater.* **2018**, *17*, 652–652. DOI: 10.1038/s41563-018-0111-8

(7) Wei, T. R.; Jin, M.; Wang, Y. C.; Chen, H. Y.; Gao, Z. Q.; Zhao, K. P.; Qiu, P. F.; Shan, Z. W.; Jiang, J.; Li, R. B.; Chen, L. D.; He, J.; Shi, X. Exceptional Plasticity in the Bulk Single-Crystalline Van Der Waals Semiconductor InSe. *Science* **2020**, *369*, 542–545. DOI: 10.1126/science.aba9778

(8) Rogers, J. A.; Someya, T.; Huang, Y. G. Materials and Mechanics for Stretchable Electronics. *Science* **2010**, *327*, 1603–1607. DOI: 10.1126/science.1182383

(9) Shi, T. F.; Chen, M. R.; Liu, Z. G.; Song, Q. F.; Ou, Y. X.; Wang, H. Q.; Liang, J.; Zhang, Q. H.; Mao, Z. D.; Wang, Z. W.; Zheng, J. Y.; Han, Q. C.; Razeeb, K. M.; Zong, P. A. A Bi_2Te_3-Filled Nickel Foam Film with Exceptional Flexibility and Thermoelectric Performance. *Nanomaterials* **2022**, *12*, 1693. DOI: 10.3390/nano12101693

(10) Loureiro, J.; Neves, N.; Barros, R.; Mateus, T.; Santos, R.; Filonovich, S.; Reparaz, S.; Sotomayor-Torres, C. M.; Wyczisk, F.; Divay, L.; Martins, R.; Ferreira, I. Transparent Aluminium Zinc Oxide Thin Films with Enhanced Thermoelectric Properties. *J. Mater*. *Chem*. *A* **2014**, *2*, 6649–6655. DOI: 10.1039/c3ta15052f

(11) Figueira, J.; Loureiro, J.; Vieira, E.; Fortunato, E.; Martins, R.; Pereira, L. Flexible, Scalable, and Efficient Thermoelectric Touch Detector Based on PDMS and Graphite Flakes. *Flex*. *Print. Electron*. **2021**, *6*, 045018. DOI: 10.1088/2058-8585/ac45de

(12) Chhowalla, M.; Shin, H. S.; Eda, G.; Li, L. J.; Loh, K. P.; Zhang, H. The Chemistry of Two-Dimensional Layered Transition Metal Dichalcogenide Nanosheets. *Nat. Chem.* **2013**, *5*, 263–275. DOI: 10.1038/nchem.1589

(13) Kanahashi, K.; Pu, J.; Takenobu, T. 2D Materials for Large-Area Flexible Thermoelectric Devices. *Adv. Energy Mater.* **2020**, *10*, 1902842. DOI: 10.1002/aenm.201902842

(14) Hicks, L. D.; Harman, T. C.; Sun, X.; Dresselhaus, M. S. Experimental Study of the Effect of

Quantum-Well Structures on the Thermoelectric Figure of Merit. *Phys. Rev. B* **1996**, *53*,

10493–10496. DOI: 10.1103/PhysRevB.53.R10493

(15) Liao, L. P.; Jiang, D. G.; Zheng, K.; Zhang, M. Z.; Liu, J. Q. Industry-Scale and

Environmentally Stable $Ti_3C_2T_x$ MXene Based Film for Flexible Energy Storage Devices. *Adv. Funct.*

Mater. **2021,** *31*, 2103960. DOI: 10.1002/adfm.202103960

(16) Lukatskaya, M. R.; Kota, S.; Lin, Z. F.; Zhao, M. Q.; Shpigel, N.; Levi, M. D.; Halim, J.;

Taberna, P. L.; Barsoum, M.; Simon, P.; Gogotsi, Y. Ultra-High-Rate Pseudocapacitive Energy

Storage in Two-Dimensional Transition Metal Carbides. *Nat. Energy* **2017**, *2*, 17105. DOI:

10.1038/nenergy.2017.105

(17) Anasori, B.; Lukatskaya, M. R.; Gogotsi, Y. 2D Metal Carbides and Nitrides (MXenes) for

Energy Storage. *Nat. Rev. Mater.* **2017**, *2*, 16098. DOI: 10.1038/natrevmats.2016.98

(18) Pan, Z. H.; Kang, L. X.; Li, T.; Waqar, M.; Yang, J.; Gu, Q. L.; Liu, X. M.; Kou, Z. K.; Wang, Z.;

Zheng, L. R.; Wang, J. Black Phosphorus@$Ti_3C_2T_x$ MXene Composites with Engineered Chemical

Bonds for Commercial-Level Capacitive Energy Storage. *ACS Nano* **2021**, *15*, 12975–12987. DOI:

10.1021/acsnano.1c01817

(19) Zhang, J. Q.; Zhao, Y. F.; Guo, X.; Chen, C.; Dong, C. L.; Liu, R. S.; Han, C. P.; Li, Y. D.;

Gogotsi, Y.; Wang, G. X. Single Platinum Atoms Immobilized on an MXene as an Efficient Catalyst

for the Hydrogen Evolution Reaction. *Nat. Catal.* **2018**, *1*, 985–992. DOI:

10.1038/s41929-018-0195-1

(20) Li, Z. D.; Attanayake, N. H.; Blackburn, J. L.; Miller, E. M. Carbon Dioxide and Nitrogen

Reduction Reactions Using 2D Transition Metal Dichalcogenide (TMDC) and Carbide/Nitride (MXene) Catalysts. *Energy Environ. Sci.* **2021**, *14*, 6242–6286. DOI: 10.1039/d1ee03211a

(21) Li, Y.; Chen, Y. P.; Guo, Z. L.; Tang, C. C.; Sa, B. S.; Miao, N. H.; Zhou, J.; Sun, Z. M. Breaking the Linear Scaling Relations in MXene Catalysts for Efficient CO_2 Reduction. *Chem. Eng. J.* **2022**, *429*, 132171. DOI: 10.1016/j.cej.2021.132171

(22) Kim, S. J.; Koh, H. J.; Ren, C. E.; Kwon, O.; Maleski, K.; Cho, S. Y.; Anasori, B.; Kim, C. K.; Choi, Y. K.; Kim, J.; Gogotsi,Y.; Jung, H.T. Metallic $Ti_3C_2T_x$ MXene Gas Sensors with Ultrahigh Signal-to-Noise Ratio. *ACS Nano* **2018**, *12*, 986–993. DOI: 10.1021/acsnano.7b07460

(23) Yun, T.; Kim, H.; Iqbal, A.; Cho, Y. S.; Lee, G. S.; Kim, M. K.; Kim, S. J.; Kim, D.; Gogotsi, Y.; Kim, S. O.; Koo, C.M. Electromagnetic Shielding of Monolayer MXene Assemblies. *Adv. Mater.* **2020**, *32*, 1906769. DOI: 10.1002/adma.201906769

(24) Cao, Y.; Zeng, Z. H.; Huang, D. Y.; Chen, Y.; Zhang, L.; Sheng, X. X. Multifunctional Phase Change Composites Based on Biomass/MXene-Derived Hybrid Scaffolds for Excellent Electromagnetic Interference Shielding and Superior Solar/Electro-Thermal Energy Storage. *Nano Res.* **2022**, *15*, 8524–8535. DOI: 10.1007/s12274-022-4626-6

(25) Ma, Y. N.; Liu, N. S.; Li, L. Y.; Hu, X. K.; Zou, Z. G.; Wang, J. B.; Luo, S. J.; Gao, Y. H. A Highly Flexible and Sensitive Piezoresistive Sensor based on MXene with Geatly Changed Interlayer Distances. *Nat. Commun.* **2017**, *8*, 1207. DOI: 10.1038/s41467-017-01136-9

(26) Naguib, M.; Kurtoglu, M.; Presser, V.; Lu, J.; Niu, J. J.; Heon, M.; Hultman, L.; Gogotsi, Y.; Barsoum, M. W. Two-Dimensional Nanocrystals Produced by Exfoliation of Ti_3AlC_2. *Adv. Mater.* **2011**, *23*, 4248–4253. DOI: 10.1002/adma.201102306

(27) Gogotsi, Y.; Anasori, B. The Rise of MXenes. *ACS Nano* **2019**, *13*, 8491–8494. DOI: 10.1021/acsnano.9b06394

(28) Dong, Y. F.; Wu, Z. S.; Zheng, S. H.; Wang, X. H.; Qin, J. Q.; Wang, S.; Shi, X. Y.; Bao, X. H. Ti$_3$C$_2$ MXene-Derived Sodium/Potassium Titanate Nanoribbons for High-Performance Sodium/Potassium Ion Batteries with Enhanced Capacities. *ACS Nano* **2017**, *11*, 4792–4800. DOI: 10.1021/acsnano.7b01165

(29) Alhabeb, M.; Maleski, K.; Anasori, B.; Lelyukh, P.; Clark, L.; Sin, S.; Gogotsi, Y. Guidelines for Synthesis and Processing of Two-Dimensional Titanium Carbide (Ti$_3$C$_2$T$_x$ MXene). *Chem. Mat.* **2017**, *29*, 7633–7644. DOI: 10.1021/acs.chemmater.7b02847

(30) Yang, S.; Zhang, P. P.; Wang, F. X.; Ricciardulli, A. G.; Lohe, M. R.; Blom, P. W. M.; Feng, X. L. Fluoride-Free Synthesis of Two-Dimensional Titanium Carbide (MXene) Using a Binary Aqueous System. *Angew. Chem. Int. Edit.* **2018**, *57*, 15491–15495. DOI: 10.1002/anie.201809662

(31) Naguib, M.; Mashtalir, O.; Carle, J.; Presser, V.; Lu, J.; Hultman, L.; Gogotsi, Y.; Barsoum, M. W. Two-Dimensional Transition Metal Carbides. *ACS Nano* **2012**, *6*, 1322–1331. DOI: 10.1021/nn204153h

(32) Ghidiu, M.; Lukatskaya, M. R.; Zhao, M. Q.; Gogotsi, Y.; Barsoum, M. W. Conductive Two-Dimensional Titanium Carbide 'Clay' with High Volumetric Capacitance. *Nature* **2014**, *516*, 78–81. DOI: 10.1038/nature13970

(33) Cain, J. D.; Azizi, A.; Maleski, K.; Anasori, B.; Glazer, E. C.; Kim, P. Y.; Gogotsi, Y.; Helms, B. A.; Russell, T. P.; Zettl, A. Sculpting Liquids with Two-Dimensional Materials: The Assembly of Ti$_3$C$_2$T$_x$ MXene Sheets at Liquid Liquid Interfaces. *ACS Nano* **2019**, *13*, 12385–12392. DOI:

10.1021/acsnano.9b05088

(34) Lyu, B.; Kim, M.; Jing, H.; Kang, J.; Qian, C.; Lee, S.; Cho, J. H. Large-Area MXene Electrode Array for Flexible Electronics. *ACS Nano* **2019**, *13*, 11392–11400. DOI: 10.1021/acsnano.9b04731

(35) Wang, X. F.; Shen, X.; Gao, Y. R.; Wang, Z. X.; Yu, R. C.; Chen, L. Q. Atomic-Scale Recognition of Surface Structure and Intercalation Mechanism of Ti_3C_2X. *J. Am. Chem. Soc.* **2015**, *137*, 2715–2721. DOI: 10.1021/ja512820k

(36) VahidMohammadi, A.; Mojtabavi, M.; Caffrey, N. M.; Wanunu, M.; Beidaghi, M. Assembling 2D MXenes into Highly Stable Pseudocapacitive Electrodes with High Power and Energy Densities. *Adv. Mater.* **2019**, *31*, 1806931. DOI: 10.1002/adma.201806931

(37) Ding, W. J.; Liu, P.; Bai, Z. Z.; Wang, Y. Y.; Liu, G. Q.; Jiang, Q. L.; Jiang, F. X.; Liu, P. P.; Liu, C. C.; Xu, J. K. Constructing Layered MXene/CNTs Composite Film with 2D-3D Sandwich Structure for High Thermoelectric Performance. *Adv. Mater. Interfaces* **2020**, *7*, 2001340. DOI: 10.1002/admi.202001340

(38) Xiong, D. B.; Li, X. F.; Bai, Z. M.; Lu, S. G. Recent Advances in Layered $Ti_3C_2T_x$ MXene for Electrochemical Energy Storage. *Small* **2018**, *14*, 1703419. DOI: 10.1002/smll.201703419

(39) Mortier, W. J.; Vangenechten, K.; Gasteiger, J. Electronegativity Equalization-Application and Papametrization. *J. Am. Chem. Soc.* **1985**, *107*, 829–835. DOI: 10.1021/ja00290a017

(40) Xia, F. J.; Lao, J. C.; Yu, R. H.; Sang, X. H.; Luo, J. Y.; Li, Y.; Wu, J. S. Ambient Oxidation of Ti_3C_2 MXene Initialized by Atomic Defects. *Nanoscale* **2019**, *11*, 23330–23337. DOI: 10.1039/c9nr07236e

(41) Sang, X. H.; Xie, Y.; Lin, M. W.; Alhabeb, M.; Van Aken, K. L.; Gogotsi, Y.; Kent, P. R. C.;

Xiao, K.; Unocic, R. R. Atomic Defects in Monolayer Titanium Carbide (Ti$_3$C$_2$T$_x$) MXene. *ACS Nano* **2016**, *10*, 9193–9200. DOI: 10.1021/acsnano.6b05240

(42) Ling, Z.; Zhou, H.; Dong, H. S.; Shi, C. R.; Zhao, J. F.; Liu, H. Q.; Song, Y. C. MXene (Ti$_3$C$_2$T$_x$) as a Promising Substrate for Methane Storage via Enhanced Gas Hydrate Formation. *J. Phys. Chem. Lett.* **2021**, *12*, 6622–6627. DOI: 10.1021/acs.jpclett.1c01649

(43) Singh, M.; Singh, A. K. Performance Improvement of Photovoltaic: Utilization of Two-Dimensional Ti$_3$C$_2$T$_x$ MXene. *Surf. Interfaces* **2021**, *27*, 101566. DOI: 10.1016/j.surfin.2021.101566

(44) Lee, Y.; Kim, S. J.; Kim, Y. J.; Lim, Y.; Chae, Y.; Lee, B. J.; Kim, Y. T.; Han, H.; Gogotsi, Y.; Ahn, C. W. Oxidation-Resistant Titanium Carbide MXene Films. *J. Mater. Chem. A* **2020**, *8*, 573–581. DOI: 10.1039/c9ta07036b

(45) Zhang, C. F. J.; Pinilla, S.; McEyoy, N.; Cullen, C. P.; Anasori, B.; Long, E.; Park, S. H.; Seral-Ascaso, A.; Shmeliov, A.; Krishnan, D.; Morant, C.; Liu, X. H.; Duesberg, G. S.; Gogotsi, Y.; Nicolosi, V. Oxidation Stability of Colloidal Two-Dimensional Titanium Carbides (MXenes). *Chem. Mat.* **2017**, *29*, 4848–4856. DOI: 10.1021/acs.chemmater.7b00745

(46) Hart, J. L.; Hantanasirisakul, K.; Lang, A. C.; Anasori, B.; Pinto, D.; Pivak, Y.; van Omme, J. T.; May, S. J.; Gogotsi, Y.; Taheri, M. L. Control of MXenes' Electronic Properties Through Termination and Intercalation. *Nat. Commun.* **2019**, *10*, 522 . DOI: 10.1038/s41467-018-08169-8

(47) Zong P. A.; Zhang P.; Yin S. J.; Huang Y. J.; Wang Y. L.; Wan C. L. Fabrication and Characterization of a Hybrid Bi$_2$Se$_3$/Organic Superlattice for Thermoelectric Energy Conversion. Adv. Electron mater. **2019**, *5*, 1800842. DOI:10.1002/aelm.201800842

(48) Zong, P. A.; Yoo, D.; Zhang, P.; Wang, Y.; Huang, Y.; Yin, S.; Liang, J.; Wang, Y.; Koumoto, K.; Wan, C. L. Flexible Foil of Hybrid TaS$_2$/Organic Superlattice: Fabrication and Electrical Properties. *Small* 2020, *16*, e1901901. DOI: 10.1002/smll.201901901

(49) Huang, Y. J.; Liang, J.; Wang, C.; Yin, S. J.; Fu, W. Y.; Zhu, H. W.; Wan, C. L. Hybrid Superlattices of Two-Dimensional Materials and Organics. *Chem. Soc. Rev.* **2020**, *49*, 6866–6883. DOI: 10.1039/d0cs00148a

(50) Zhang, T.; Pan, L. M.; Tang, H.; Du, F.; Guo, Y. H.; Qiu, T.; Yang, J. Synthesis of Two-Dimensional Ti$_3$C$_2$T$_x$ MXene Using HCl Plus LiF Etchant: Enhanced Exfoliation and Delamination. *J. Alloy. Compd.* **2017**, *695*, 818–826. DOI: 10.1016/j.jallcom.2016.10.127

(51) Wan, C. L.; Tian, R. M.; Azizi, A. B.; Huang, Y. J.; Wei, Q. S.; Sasai, R.; Wasusate, S.; Ishida, T.; Koumoto, K. Flexible Thermoelectric Foil for Wearable Energy Harvesting. *Nano Energy* **2016**, *30*, 840–845. DOI: 10.1016/j.nanoen.2016.09.011

(52) Zhang, Z. R.; Yao, Z. P.; Zhang, X.; Jiang, Z. H. 2D Carbide MXene Under Postetch Low-Temperature Annealing for High-Performance Supercapacitor Electrode. *Electrochim. Acta* **2020**, *359*, 136960. DOI: 10.1016/j.electacta.2020.136960

(53) Ruby, C.; Ott, R.; Huang, F.; Weaver, M. L.; Barnard, J. A. XPS Study of Reactively Sputtered Ti-B-N Hard Coatings. *Surf Interface Anal* **2000**, *29*, 823–828. DOI: 10.1002/1096-9918(200012)29:12<823::Aid-sia933>3.0.Co;2-c

(54) Hendrickson, D. N.; Hollander, J. M.; Jolly, W. L. Nitrogen 1s Electron Binding Energies Correlation with Molecular Orbital Calculated Nitrogen Charges. *Inorg. Chem.* **1969**, *8*, 2642–2647. DOI: 10.1021/ic50082a020

(55) Liu, P.; Ding, W. J.; Liu, J.; Shen, L. L.; Jiang, F. X.; Liu, P. P.; Zhu, Z. Y.; Zhang, G.; Liu, C. C.; Xu, J. K. Surface Termination Modification on High-Conductivity MXene Film for Energy Conversion. *J. Alloy. Compd.* **2020**, *829*, 154634. DOI: 10.1016/j.jallcom.2020.154634

(56) Luo, J. M.; Matios, E.; Wang, H.; Tao, X. Y.; Li, W. Y. Interfacial Structure Design of MXene-Basednanomaterials for Electrochemical Energy Storage and Conversion. *InfoMat* **2020**, *2*, 1057–1076. DOI: 10.1002/inf2.12118

(57) Lipatov, A.; Alhabeb, M.; Lukatskaya, M. R.; Boson, A.; Gogotsi, Y.; Sinitskii, A. Effect of Synthesis on Quality, Electronic Properties and Environmental Stability of Individual Monolayer Ti_3C_2 MXene Flakes. *Adv. Electron. Mater.* **2016**, *2*, 1600255. DOI: 10.1002/aelm.201600255

(58) Amano, F.; Nakata, M. High-Temperature Calcination and Hydrogen Reduction of rRutile TiO_2: A Method to Improve the Photocatalytic Activity for Water Oxidation. *Appl. Catal. B-Environ.* **2014**, *158*, 202–208. DOI: 10.1016/j.apcatb.2014.04.025

(59) Wang, P. L.; Kolodiazhnyi, T.; Yao, J. L.; Mozharivskyj, Y. Decoupling the Electrical Conductivity and Seebeck Coefficient in the RE_2SbO_2 Compounds through Local Structural Perturbations. *J. Am. Chem. Soc.* **2012**, *134*, 1426–1429. DOI: 10.1021/ja209652d

(60) Peng, J.; Snyder, G. J. A Figure of Merit for Flexibility. *Science* **2019**, *366*, 690–691. DOI: 10.1126/science.aaz5704

(61) Hantanasirisakul, K.; Zhao, M. Q.; Urbankowski, P.; Halim, J.; Anasori, B.; Kota, S.; Ren, C. E.; Barsoum, M. W.; Gogotsi, Y. Fabrication of $Ti_3C_2T_x$ MXene Transparent Thin Films with Tunable Optoelectronic Properties. *Adv. Electron. Mater.* **2016**, *2*, 1600050. DOI: 10.1002/aelm.201600050

(62) Lee, S.; Kim, E. H.; Yu, S.; Kim, H.; Park, C.; Park, T. H.; Han, H.; Lee, S. W.; Baek, S.; Jin, W.

Alternating-Current MXene Polymer Light-Emitting Diodes. *Adv. Funct. Mater.* **2020**, *30*, 2001214. DOI: 10.1002/adfm.202001224

(63) Yang, K.; Yin, F. X.; Xia, D.; Peng, H. F.; Yang, J. Z.; Yuan, W. J. A Highly Flexible and Multifunctional Strain Sensor Based on a Network-Structured MXene/Polyurethane Mat with Ultra-High Sensitivity and a Broad Sensing Range. *Nanoscale* **2019**, *11*, 9949–9957. DOI: 10.1039/c9nr00488b

(64) Tang, H. H.; Feng, H. R.; Wang, H. K.; Wang, X. J.; Liang, J. J.; Chen, Y. Highly Conducting MXene-Silver Nanowire Transparent Electrodes for Flexible Organic Solar Cells. *ACS Appl. Mater. Interfaces* **2019**, *11*, 25330–25337. DOI: 10.1021/acsami.9b04113

(65) Wang, K.; Zhou, Y. F.; Xu, W. T.; Huang, D. C.; Wang, Z. G.; Hong, M. C. Fabrication and Thermal Stability of Two-Dimensional Carbide Ti_3C_2 Nanosheets. *Ceram. Int.* **2016**, *42*, 8419–8424. DOI: 10.1016/j.ceramint.2016.02.059

(66) Tian, R. M.; Wan, C. L.; Wang, Y. F.; Wei, Q. S.; Ishida, T.; Yamamoto, A.; Tsuruta, A.; Shin, W. S.; Li, S.; Koumoto, K. A Solution-Processed TiS_2/Organic Hybrid Superlattice Film towards Flexible Thermoelectric Devices. *J. Mater. Chem. A* **2017**, *5*, 564–570. DOI: 10.1039/c6ta08838d

Graphic for manuscript

Superlattice

Power generation